2023 IEEE International Conference on Robotics and Automation (ICRA 2023)
May 29 - June 2, 2023. London, UK

Exploring An External Approach to Subretinal Drug Delivery via Robot Assistance and B-Mode OCT

Elan Z. Ahronovich[1], Neel Shihora[1], Jin-Hui Shen[2], Karen Joos[2], Nabil Simaan[1†]

***Abstract*— Injections into specific retinal layers of the eye present a serious challenge to surgeons in terms of accuracy and perception. The emergence of new gene therapies further emphasizes the need for effective tools for localized drug delivery. Unlike the dominant approach of delivering drugs via a transvitreal intraocular pathway, this paper demonstrates the feasibility of delivering injections into the space between the choroid and the retina using an external approach. The design of a cooperative robotic system for enabling robot-assisted extraocular subretinal injections is presented. The system uses a distal micromanipulator that can serve as a hand-held tool for OCT-aided injection or attach to a six degree of freedom (DOF) serial robot arm for cooperative manipulation. The kinematics and control of the robot for constrained cooperative control motions to enable safe needle injection is presented and experimentally evaluated. These results suggest that the proposed external drug delivery approach is feasible, thereby enabling the advantages of preserving the integrity of the retina and omitting the necessity for vitrectomy.**

***Index Terms*— Serial robots, kinematics, OCT, cooperative control**

I. Introduction

Injectable gene therapies are being developed to treat retinal degeneration caused by age-related ocular diseases [1], [2]. Some of these therapies rely on subretinal injections for localized drug delivery. These types of injections require extreme precision in controlling needle depth for safeguarding against trauma to underlying retinal anatomy. Manual tremor is a key challenge to achieving safe drug delivery, but it is not the only one. The ability to control the depth and the volume of injected drugs are important factors in limiting the risk of retinal detachment, retinal tears, and subretinal bleeding. The costly nature and efficacy of these gene therapies highlight the need for new technologies that enable their safe delivery for retinal diseases. This need motivated the development of a system of co-dependent technologies (optical coherence tomography (OCT) and robotics) for enabling safe and repeatable external trans-scleral subretinal drug delivery.

Currently, an intraocular approach (ⓘ in Fig. 1) to subretinal drug delivery is the only practiced technique, which offers limited visualization from surgical microscopy through a dilated iris. Besides vision difficulties, intraocular dexterity is very constrained when using long rigid tools through scleral trocars. Figure 1 shows the cross-section and labeled layers of the retina with the top portion of the cross-section representing the intraocular retinal layer. Injectable gene therapies target particular retinal layers (e.g. Voretigene neparvovec targets the Retinal Pigment Epithelium (RPE)), which, if approached internally requires puncturing several retinal layers that are highly susceptible to tearing and bleeding that can lead to irreparable vision impairment. This paper presents a novel external trans-scleral technique (ⓔ in Fig. 1) to deliver subretinal injections by approaching the RPE from the anterior of the eye, thereby circumventing the above surgical challenges by using a robot-attached tool with OCT visual guidance.

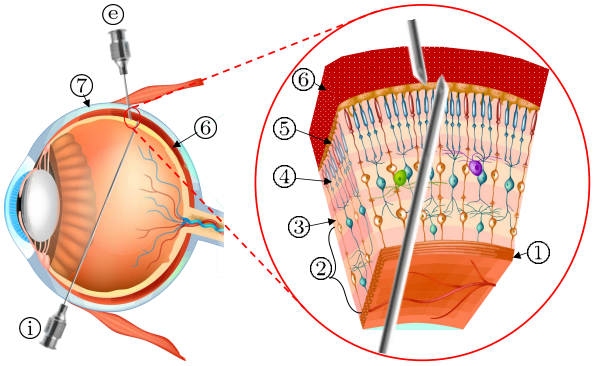

Fig. 1. Two approaches to drug delivery: ⓘ internal approach, ⓔ external approach. Also shown are the relevant layers of the eye: ① Internal limiting membrane, ② Ganglionic layer, ③ external limiting membrane, ④ Rods & cones, ⑤ retinal pigment epithilium (RPE), ⑥ choroid, ⑦ sclera.

Approaching the RPE from the exterior of the eye provides several benefits to both surgeon and patient and presents a new paradigm of therapeutic drug delivery for ocular diseases. Eliminating the need for scleral trocars by using an external approach fundamentally changes the way a surgeon manipulates the eye, in turn decreasing procedural difficulty. Although traditional microscopy can still be used to aid the surgeon with needle targeting, the benefits of this proposed technique are provided by the use of OCT producing cross sectional imagery of the retina. Unlike microscopy, with OCT the surgeon is able to differentiate specific retinal layers to precisely target drug delivery. Due to the sensitivity of retinal tissue, limiting extraneous needle movements throughout the injection time period is paramount in minimizing patient trauma and maximizing the delivered drug volume. The presented robotic system shares control of surgical tools with the surgeon. This enables filtering physiological tremor while simultaneously providing the framework to enable

† Corresponding author
[1]Department of Mechanical Engineering, Vanderbilt University, Nashville, TN 37235, USA (elan.z.ahronovich, nabil.simaan) @vanderbilt.edu
[2] Vanderbilt Eye Institute, Vanderbilt University Medical Center, Nashville, TN 37232
This work was supported in part by the National Institute of Health National Eye Institute grant 1R01EY02813

virtual fixtures used to limit needle puncture depth and adjust human-robot interaction parameters. While existent cooperative robotic systems similarly offer tremor filtration, the work presented here adds the capability to adjust interaction parameters based on visual feedback to further improve procedural success rates and patient outcomes.

Another advantage to the external approach is safety in the case of accidental eye movement (e.g. due to patient coughing). In an internal approach, a needle crosses through the eye to reach the posterior regions and would therefore need to be rapidly retracted. In contrast, when resting the robot tip against the sclera in the external approach the needle advances only a small amount into the target subretinal layer. In the event of accidental eye movement, the needle has a smaller distance to travel when retracting, reducing the likelihood of internal retinal trauma.

In light of the above clinical needs, and prior works listed in the next section, this paper presents a contribution demonstrating the first known external approach for subretinal drug delivery using B-mode OCT imagery and cooperative robot assistance. We discuss the challenges involved with collaborative micro-manipulation and in providing OCT-based robot stabilization. Additionally, the paper presents surgical tool gravitational compensation, and an OCT-informed variable admittance control law.

II. Relevant Works

Recent reviews of robotics for ophthalmic surgery can be found in [3], [4]. The literature, in large, presents four distinct categories of robotic systems aimed at aiding in vitreoretinal surgery: 1) telemanipulation; 2) handheld; 3) magnetically controlled; and 4) cooperatively controlled. Telemanipulated robots offer tremor filtering by physically detaching the user's control input from the robot performing a particular task in a leader-follower architecture. The PRECYES Surgical System [5], The Intraocular Robotic Interventional Surgical System (IRISS) [6] and Wei et al. [7] are examples of telemanipulated surgical assistants for vitreoretinal surgery.

Handheld robotic devices are designed to minimize the disruption of surgical flow with devices entirely encapsulated in handheld packages, the Micron system [8] for instance, with micro-actuators respond to filter a user's tremor.

Magnetically controlled robots [9] employ magnetic fields to drive drug-eluding intraocular micro-robots offering a solution completely independent of the human-effect.

Cooperatively controlled robots offload the burden of carrying tools and offer tremor filtering while allowing the user to command motions via force/moment cues applied to the tool. The Johns Hopkins Steady-Hand Eye Robot (SHER) [10] and the work from Gijbels et al. [11] are both relevant examples of vitreoretinal cooperative robotic systems.

Additionally, the literature presents the combination of intraocular OCT with robotic tools. OCT signal can be used to visualize tissue with a 1D-image (A-mode) which is typically used for depth information, a 2D-image (B-mode) or a 3D-image (C-mode) [12]. Song et al. [13] developed a handheld one degree of freedom (DoF) robotic device that used A-mode OCT to control the distance of a needle to a target and Kang et al. [14] demonstrated the capability to perform subretinal injections with the aid of A-mode OCT. Ourak et al. [15] used A-mode OCT for feedback in controlling distance in a robotic system. Yu et al. [16], [17] used custom vitreoretinal forceps with B-mode OCT imagery on a telemanipulated robotic device for epiretinal membrane peeling and Del Giudice et al. [18] showed that using continuum robots for equilibrium modulation (CREM) can produce high fidelity C-mode OCT scans.

III. Robotic System for Microsurgery

Depending on user preference and task precision requirements, a surgeon may prefer to use a robotic handheld tool or a hand-in-hand (cooperative) approach whereby the tool is attached to a robot that is guided through force cues. Since it is yet unclear what the eventual user preference will be for the task of subretinal injection using the external approach, we designed a modular system that we call *CORA* (Cooperative OCT-guided Robotic Assistant) that offers two modes of operation: Mode 1 is a handheld robot assistant to control depth and injection volume offering OCT visual feedback to the user; Mode 2 is a cooperative robot with selective compliance, tremor filtering, and OCT-based visual servoing for attractive virtual fixtures. The following is a description of this system.

A. Mode 1: Handheld robotic tool

The main purpose of the Mode 1 robotic tool, in Fig. 2, is to assist in the tasks of needle depth control, stabilization of the tool in the needle direction, injection volume control, and to enable simultaneous visualization of the needle and anatomy using B-mode OCT. The tool weighs 220 grams and is designed to rest in the crook of the user's thumb with a precision pinch grip. The tool can be mounted on the Mode 2 robot using a quick-connect interface as described below.

The tool is comprised from a single-axis anti-backlash linear actuator ①, a B-mode OCT probe ② with a custom 36 gauge needle ③, and a scleral stabilization horn ④. The function of the scleral stabilization horn is to allow the surgeon to brace the tip of the tool against the sclera. If the user desires, a foot-pedal enables fine advancement of the needle to the target subretinal layer. The volume injection is controlled using a programmable pump Fig. 2 (d) that is activated by a separate switch once the subretinal layer is reached.

The custom B-mode OCT probe shown in Fig. 3(a) is a variation of the design presented in [19] with the OCT fiber oriented to visualize the needle and tissue as shown in Fig. 3(b)(c). To acquire B-mode OCT images the probe produces a lateral oscillation of an optic fiber with a GRIN lens using a 1300 nm wavelength. The probe produces B-mode OCT images with 5 to 30 Hz B-mode frequency. The OCT engine is a THORLABS VEGA 210C1 Swept Source OCT System and displays the image on a computer (Intel®

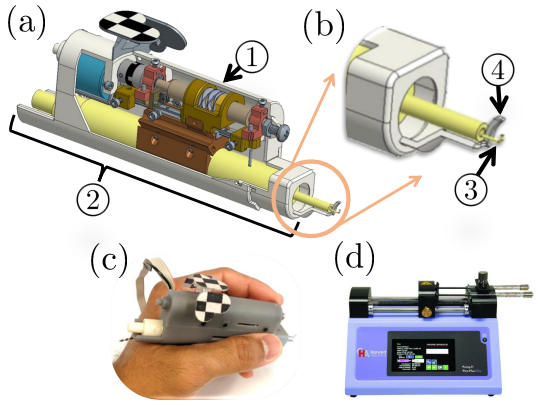

Fig. 2. (a) CAD design of the Mode 1 handheld device highlighting the ① anti-backlash nut and the ② Custom B-mode OCT probe. (b) Details of the ③ 36 gauge needle and ④ scleral stabilization horn. (c) Representation of how a user holds the tool and (d) Programmable Pump (Harvard Apparatus Standard Infuse/Withdraw Pump 11 Pico Plus Elite Programmable Syringe Pump) for automated injection of precisely 15μl.

Xeon® E3-1270 v5 @ 3.60 GHz) running a custom MATLAB script that calculates the distance between two user-selected regions of interest (ROI). The distance between the ROIs is sent to the robot control computer via user datagram protocol (UDP) at an average of 23 Hz to adjust admittance gains. We found this UDP frequency to be sufficient to not introduce control lag with robot end effector speeds at several mm/s.

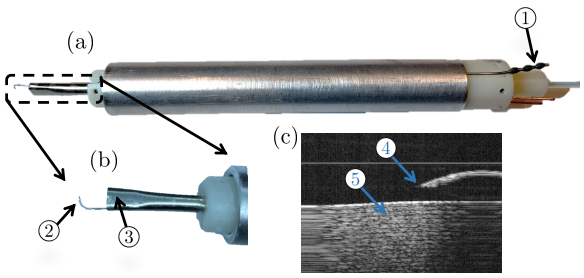

Fig. 3. (a) Custom B-mode OCT Probe with ① drug delivery channel. (b) Details of the probe tip with ② 90° needle for sub-retinal injection and ③ optical fiber proximal to the needle transmitting OCT image (c) of the ④ needle and ⑤ target tissue.

B. Mode 2 robot

CORA is shown in Fig. 4. It is a 7 DoF cooperative robotic system for OCT-guided vitreoretinal procedures. It includes a 6 DoF serial robot arm (Meca500, Mecademic, Montreal, Quebec, Canada), the 1 DoF handheld Mode 1 device, and two 6 DoF force/torque (F/T) sensors. The Mode 1 device assembles as a cartridge to the robot with a single screw and safety latch that can be assembled/disassembled in a few seconds. A surgeon co-manipulates the Mode 1 device when assembled in the robot by grasping the tool in the same fashion as if without the robot. Their input wrench is measured by one F/T sensor (ATI Mini 40, ATI Industrial Automation, Apex, NC, USA) to determine robot end effector velocity.

Control of The Meca500 robot is from a custom Simulink Real-Time™ code communicating using EtherCAT on a control loop frequency of 1KHz on an Intel ® Core™2 Duo E7400 @ 2.80 GHz. The F/T sensors are sampled via UDP and passed through a 30 point moving average filter. The user interface includes a screen showing the OCT view and another screen showing the microscope view which will be simultaneously displayed onto a TrueVision 3D Surgical System for enucleated eye and in-vivo experiments. The control of the Meca500 was carried out using joint-level velocity control based on velocity reference commands produced via an admittance equation as described in Section IV-A. The Meca500's control interface includes the parameter called *SetVelTimeout* which sets the length of time the robot honors a particular velocity command before joint velocities are set to zero, unless another velocity command is sent. We set this timeout value to 1ms to ensure safe and stable behavior in the case of corrupt communication.

The user has the freedom to switch between three control modes: 1) free space 6 DoF control with orientation and position control of the end effector, 2) Cartesian space control (fixed tool orientation), and 3) Orientation control (fixed tool tip position effectively enforcing a remote center of motion by software). While using any of these three control modes with the feedback from OCT imagery, we are able to establish virtual fixtures to guide the user in limiting the needle puncture depth.

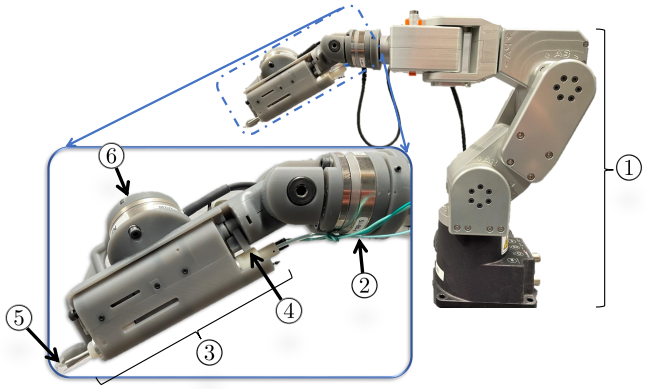

Fig. 4. Cooperative robotic system with ① Meca500 6-axis industrial robot, ② ATI Mini40 6-axis load cell for user input to admittance control, ③ Mode 1 handheld device with OCT probe, ④ safety latch for the Mode 1 device, ⑤ custom 36 gauge needle and scleral stabilization horn, and ④ ATI Nano43 6-axis load cell for scleral interaction forces.

IV. Kinematics and Cooperative Control

In Section III-B the robotic system is described and the following discussion presents the kinematics dictating the end effector motion with cooperative control of the surgical tool with the aid of virtual fixtures. The frame assignment used for the Meca500's forward kinematics are shown in Fig. 5 where the user's frame[1] of reference (ie. world coordinate

[1]The notation {A} denotes a right-handed frame with origin $\mathbf{o}_a$ and unit vectors $\hat{\mathbf{x}}_a, \hat{\mathbf{y}}_a, \hat{\mathbf{z}}_a$

system, wcs) is frame {W}. It is important to note the distinction between the wcs and the estimated point at which the user physically interacts with the robot, {g}, which is used for the wrench transformation and defining the motion reference point within the kinematics equations.

When an individual manipulates a long slender needle in space, intended needle tip velocities are administered by imposing a wrench at the gripping point. The human in the loop unconsciously does the transformation of desired needle tip speed from their gripping point. We leverage this automatic conversion and directly calculate a velocity of the gripping point and tune admittance parameters to establish an appropriate force-velocity scaling of the needle tip to match the user's intentions.

Joint	$\mathbf{a}_i$	$\boldsymbol{\alpha}_i$	$\mathbf{d}_i$	$\boldsymbol{\theta}_i$
1	0	−90	135	q_1
2	135	0	0	q_2
3	38	−90	0	q_3
4	0	90	120	q_4
5	0	−90	0	q_5
6	0	0	70	q_6

Transform	$\mathbf{a}_i$	$\boldsymbol{\alpha}_i$	$\mathbf{d}_i$	$\boldsymbol{\theta}_i$
{6}-{T_1}	0	90	e_1	0
{T_1}-{G}	k	−90	0	θ

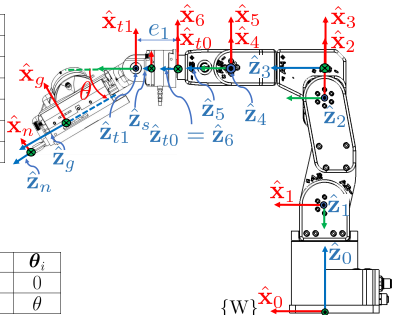

Fig. 5. Frame assignment for Meca500 robot and attached surgical tool. The D-H table denotes linear offsets $\mathbf{a}_i$ and $\mathbf{d}_i$ in mm. Frame {G} denotes the frame where the user grasps the combined robotic needle & OCT tool. Frame {S} designates the F/T sensor frame.

The instantaneous kinematics of the robot is given by $\mathbf{J}\dot{\mathbf{q}} = \dot{\mathbf{x}}$ where $\mathbf{J}$ is the robot Jacobian derived with the origin of frame $\{G\}$ as the end-effector (since the user grasps the robot at $\mathbf{o}_g$), $\dot{\mathbf{x}}$ is the end effector twist with linear velocity preceding angular velocity, and $\dot{\mathbf{q}} \in \mathbb{R}^6$ are the joint speeds.

The twist $\dot{\mathbf{x}}$ is a known parameter determined by the user's input wrench via an admittance control law. Given this twist, we solve for the robot joint velocities as $\dot{\mathbf{q}} = \mathbf{J}^\dagger \dot{\mathbf{x}}$ where $\mathbf{J}^\dagger$ is the singularity robust pseudo-inverse [20] of $\mathbf{J}$:

$$\mathbf{J}^\dagger = \mathbf{W}^{-1}\mathbf{J}^{\mathrm{T}}\left(\mathbf{J}\,\mathbf{W}^{-1}\mathbf{J}^{\mathrm{T}} + \alpha^2\,\mathbf{I}\right)^{-1} \tag{1}$$

where $\mathbf{W} = \mathrm{diag}([1, 1, 50, 50, 1, 1])$ is a weighting matrix acting to preferentially restrict the motions of joints three and four to decrease the motion envelope of the robot arm. These weighting values were estimated and tested in simulation then finalized with experimental validation using the robot. α is the singularity robustness parameter determined based on the manipulability of the robot in a way that gradually increases the singularity robustness parameter as the robot approaches singularity:

$$\alpha = \begin{cases} \alpha_0\left(1 - \frac{\mu}{\mu_0}\right)^2 & \mu < \mu_0 \\ 0 & \mu > \mu_0 \end{cases} \tag{2}$$

where $\mu = \sqrt{\det(\mathbf{J}\mathbf{J}^{\mathrm{T}})} \in \mathbb{R}$ is the robot's manipulability, $\mu_0 = 0.0001$ is a reference manipulability calculated when the robot is in a poorly conditioned configuration (2° away from the robot's elbow singularity). The parameter $\alpha_0 = 0.2$ was set experimentally for a twist with units of [mm/s] for liner velocity components.

A. Cooperative Control

The aim of admittance control in this work is to provide a human-robot interaction that responds naturally to user commands to reduce the learning curve while maximizing the benefit of cooperative manipulation. OCT-based variable admittance is leveraged to maximize the benefit of cooperative manipulation by assisting the user in safely approaching a target injection layer.

The F/T sensor frame {S} is rotated by 22.5° about the axis perpendicular to the robot's end-effector flange ($\hat{\mathbf{z}}_6$). Assuming the orientation of frame {6} is given by ${}^0\mathbf{R}_6$ as obtained from direct kinematics, the orientation of the sensor frame is given by[2]:

$${}^w\mathbf{R}_s = {}^0\mathbf{R}_6\left[e^{(\pi/8[\mathbf{e}_3]^\wedge)}\right], \quad \mathbf{e}_3 \triangleq [0,0,1]^{\mathrm{T}} \tag{3}$$

Since the user input wrench is applied to the gripping point $\mathbf{o}_g$ (origin of frame $\{G\}$) and read by the F/T sensor in the sensor frame $\{S\}$ the motion and forces by the user need to be represented in a frame $\{\tilde{G}\}$ centered at $\mathbf{o}_g$ and parallel to the wcs {W}. Therefore[3], the sensed wrench ${}^s\mathbf{w}$ is transformed to its representation ${}^{\tilde{g}}\mathbf{w}$ in $\{\tilde{G}\}$ using:

$${}^{\tilde{g}}\mathbf{w} = {}^w\mathbf{T}_s\,{}^s\mathbf{w}, \quad {}^w\mathbf{T}_s = \begin{bmatrix} {}^w\mathbf{R}_s & \mathbf{0} \\ {}^w\mathbf{p}_{s/g} \times {}^w\mathbf{R}_s & {}^w\mathbf{R}_s \end{bmatrix} \tag{4}$$

where ${}^w\mathbf{p}_{s/g}$ is the vector from the gripping point to the origin of {S}.

After computing the user's wrench in $\{\tilde{G}\}$, the control reference end effector twist $\dot{\mathbf{x}} \in \mathbb{R}^6$ is computed by scaling the user's force input as:

$${}^w\dot{\mathbf{x}}_{\mathrm{des}} = \mathbf{K}\,{}^w\mathbf{T}_s\,{}^s\mathbf{w}, \quad \mathbf{w} \triangleq [\mathbf{f}^{\mathrm{T}}, \mathbf{m}^{\mathrm{T}}]^{\mathrm{T}}, \mathbf{f}, \mathbf{m} \in \mathbb{R}^3 \tag{5}$$

where $\mathbf{K} = \mathrm{diag}([k_{\mathrm{f}}, k_{\mathrm{f}}, k_{\mathrm{f}}, k_{\mathrm{m}}, k_{\mathrm{m}}, k_{\mathrm{m}}])$ and scalars k_{f} and k_{m} are force and moment gains, respectively.

To avoid user frustration by using the small admittance gain needed for slow motions and tremor filtering, we implemented a variable admittance law. This law uses a soft step function to allow fast motions for large force magnitudes and to enforce slow motions for small force magnitudes. To achieve this, we compute the force and moment ratios $\tau_f \triangleq ||\mathbf{f}||/f_{max}$ and $\tau_m = ||\mathbf{m}||/m_{max}$, respectively, where $f_{max} = 6N$ and $m_{max} = 400Nmm$. Using these two ratios, we compute the gains k_f and k_m using the following equation with $\tau = \tau_f$ for k_f and $\tau = \tau_m$ for k_m:

$$k = \begin{cases} k_{\min} + \frac{(k_{\max} - k_{\min})(1 + \tanh(\pi\nu(\tau - 0.25)))}{2} & \tau > \tau_0 \\ 0 & \tau \leq \tau_0 \end{cases} \tag{6}$$

where $k_{\max}$ is a preset maximum gain value determined based on user comfort and robot stability, $k_{\min} = \frac{k_{\max}}{\rho}$ (ρ is a user set divisor), $\nu = 3$ is a smoothing factor for the extrema of the hyperbolic tangent function. We used $k_{\max}$

[2]The notation $[\mathbf{v}]^\wedge$ denotes the cross-product matrix of vector $\mathbf{v} \in \mathbb{R}^3$.
[3]We use ${}^a\mathbf{v}$ to represent vector $\mathbf{v}$ as represented in frame {A}

as 20 (mm/Ns) or 15 (mm/Ns) for force and $k_{\max}$ as 0.0001 (deg/Nmm sec) for moment where the different values were determined per user preference. ρ was set at 15 for forces and 20 for moments.

The threshold value τ_0 was set at $0.1N$ for force and $45Nmm$ for moment. These thresholds are needed to ensure no drift due to F/T measurement noise and uncertainty in calibrating the center of mass and mass of the tool attached to the robot. Details about the calibration of the tool mass and center of mass are found in Appendix I.

B. OCT-Based Variable Admittance Cooperative Control

With the integration of OCT imagery, the user is able to select target regions (e.g. the RPE of the retina) for drug delivery and further modulate robot control. Although the admittance gains k_{max} in Eq. (6), are set by the user for comfort, we regulate these values proportionately to the distance between the injection needle and target location based on OCT feedback. This provides a proximity-aware assistance to the user to support finer motion control and increased safety by limiting the motions of the robot when close to target injection layer.

The ROIs are tracked in OCT images via template matching as in [21]. The distance between the centers of these ROIs in the OCT's scanning plane, $\{N\}$ in Fig. 5 and their distance, η is reported with respect to that frame. To endow (6) with proximity awareness, we adjust $k_{\max}$ based on:

$$k'_{\max} = \begin{cases} k_{\max}\frac{\eta}{\eta_0} & \eta < \eta_0 \\ k_{\max} & \eta \geq \eta_0 \end{cases} \tag{7}$$

where η_0 is a pre-defined error threshold of $0.6mm$.

Registration of the angle of the OCT plane with respect to the robot is done visually by using a Near Infrared Sensor Card which allows us to see with the naked eye the direction of the scanning plane. Lastly, the segmentation script reports ROI distance in pixels which is converted to mm by imaging an object of known dimension to find the pixel-to-millimetric conversion which for this case is $195.556\frac{px}{mm}$.

V. Experimental Evaluation

To quantify the performance of *CORA*, a user study with four participants was designed comparing the performance of two tasks: path tracing and approaching a surface.

For the task of path tracing we had two conditions: 1) handheld Mode 1 tool, and 2) CORA assistance using force-based admittance in (6). In both conditions, users were asked to trace with a needle a 1.25mm square on a grid shown in Fig. 6. The needle with custom optical marker were displayed on a computer using a PointGrey FireFly2 camera with a 14x lens magnification for the user to visualize the task, refer to the multimedia extension for more detail. Six separate trials were conducted for each user, randomly ordered, per condition. The root mean square (RMS) error of the needle tip to the intended path was measured using a custom image segmentation script identifying the marker fixed to the needle. Users were allowed to practice following the path manually and with the robot as many times as was necessary to feel comfortable.

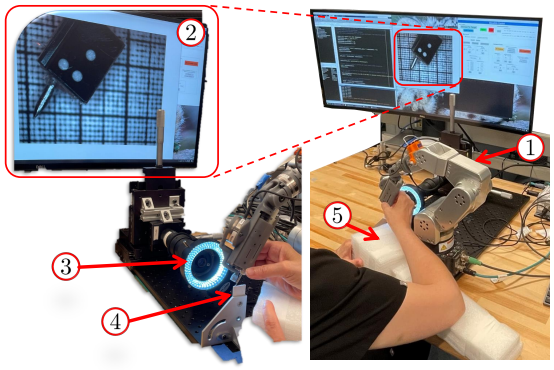

Fig. 6. The experimental setup for Mode 1 and Mode 2 path tracing. ① CORA robot, ② microscope camera view, ③ microscope camera ④ 125 micron grid paper, ⑤ arm rest.

For each path following trial, 350 frames were used to register the needle tip to the intended path as shown in Fig. 8. The RMS error of points to their nearest path edge is averaged for each user's trial and the collective data set is shown in Fig. 7. The maximum RMS errors across trials were $260\mu m$ and $125\mu m$ during handheld motion and robotic assistance, respectively - demonstrating accuracy benefits when using CORA.

The second task (approaching a surface) was designed to emulate a scenario similar to what is required for safe drug delivery. Users were instructed to touch the tip of the needle to the surface without penetrating the surface. Each user repeated the task 10 times using three conditions: 1) handheld, 2) CORA with force-based admittance gains using (6), 3) OCT distance-aware admittance using (6) and (7), as demonstrated in the multimedia extension. When users deemed the needle to be at the surface, an assistant took a snapshot of the OCT image to be manually segmented to measure distance from the needle tip to the surface.

Table I reports the surface approach results as a percent of trials that led to puncturing the surface and the error between the needle tip and surface as measured by the OCT. This table clearly demonstrates the benefit of the distance-aware admittance using OCT feedback in significantly reducing percentages of surface penetration and reducing distance of excursion into the agar. Also, this assistive mode put all users at the same performance level despite significant disparities in their manual performance.

TABLE I

Surface penetration % and (Surface approach error in μm).

User	Handheld	Force-based admittance (using (6)).	OCT-guided admittance (using (6) and (7)).
1	50% (126.9)	50% (39.4)	10% (26.7)
2	60% (130.7)	50% (47.1)	20% (30.7)
3	70% (59.6)	70% (30.3)	30% (26.5)
4	60% (55.3)	50% (34.9)	20% (22.7)

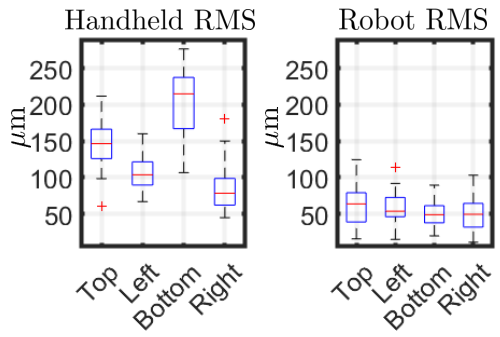

Fig. 7. Box-whisker plots for handheld and robotic path tracing experiments categorized by side of desired path. The boxes cover the 25^{th} to 75^{th} percentiles of data, the center red line indicates the median, and outliers, plotted with the red cross, are outside 2.7 standard deviations. The dashed lines indicate the maximum and minimum values.

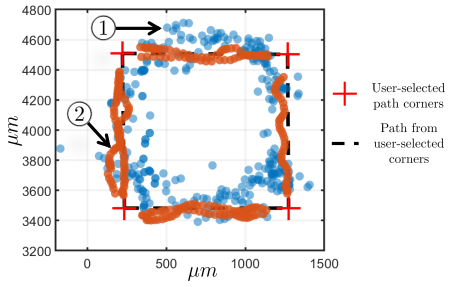

Fig. 8. Needle tip positions plotted for the path following experiment ① in orange using the Mode 1 device manually and ② in blue with the Mode 1 device assembled to CORA using admittance control.

VI. Conclusions

There is a need for new technology to enable accurate drug delivery for retinal treatment. Past approaches focused on transvitreal intraocular access, but at the cost of trauma to the retina and its underlying anatomy and necessitating vitrectomy. This paper presented a robotic system capable of using distance-aware variable admittance gains based on B-Mode OCT feedback. Both force-based and distance-aware variable gain control laws were compared against manual unaided user performance. As expected, the use of the presented robot benefited path following performance. In addition, the distance-aware OCT-based cooperative admittance law significantly improved user performance in regulating a needle tip to a target surface. We believe the technology presented in this paper will enable a less traumatic and more accurate approach to drug delivery and support the development and testing of current and future gene therapies to prevent blindness.

Appendix I
Gravity Compensation

The Mode 1 device with OCT needle is attached to a Mini40 load cell, therefore, the gravity force affects the force measurements. Compensating the gravitational effect is a two fold problem. First the attached tool's mass and the center of gravity (cg) must be identified and second, the gravitational force needs to be filtered from all force measurements to isolate the user's input. The following describes how, with a collection of wrench measurements from positioning the robot in a set of predetermined arbitrary positions, the mass of the attached device and location of its cg are determined by fitting a sphere to point cloud data as shown in [22].

The measured wrench from the force sensor can be defined as $\tilde{\mathbf{f}} = \mathbf{f} + \mathbf{o}$ where $\mathbf{f}$ is the *true wrench* applied to the load cell (e.g. a user's force input) and $\mathbf{o}$ is the bias vector $\mathbf{o} = [\frac{a}{2}, \frac{b}{2}, \frac{c}{2}]$ where the coefficients *a,b,c* are from the equation of a sphere described below. Expanding the measured wrench gives:

$$\tilde{f}_x^2 + \tilde{f}_y^2 + \tilde{f}_z^2 = \underbrace{2\tilde{f}_x o_x}_{a\tilde{f}_x} + \underbrace{2\tilde{f}_y o_y}_{b\tilde{f}_y} + \underbrace{2\tilde{f}_z o_z}_{c\tilde{f}_z} + \underbrace{(f_x^2 + f_y^2 + f_z^2 - o_x^2 - o_y^2 - o_z^2)}_{d} \tag{8a}$$

$$a\tilde{f}_x + b\tilde{f}_y + c\tilde{f}_z + d = \tilde{f}_x^2 + \tilde{f}_y^2 + \tilde{f}_z^2 \tag{8b}$$

For *n* poses of the robot with attached Mode 1 device we solve the following for $\mathbf{x}$:

$$\mathbf{A}\mathbf{x} = \mathbf{Y} \tag{9}$$

where $\mathbf{A} = [\tilde{f}_{x(k)}, \tilde{f}_{x(k)}, \tilde{f}_{x(k)}, 1]$ for $k = [1, \ldots, n]$ is a matrix of the force measurements from the load cell and, $\mathbf{x} = [a, b, c, d]^T$ is the vector of coefficients from Eq. (8a).

From the definition of d in Eq. (8a) the mass of the tool can be solved for using Newton's second law:

$$m = \frac{1}{g}\sqrt{d + o_x^2 + o_y^2 + o_z^2} = \frac{1}{g}\sqrt{d + \frac{a^2 + b^2 + c^2}{4}} \tag{10}$$

The moment imposed by the tool on the sensor is defined as:

$$\tilde{\mathbf{m}} = {}^s\mathbf{r} \times (mg)\hat{\mathbf{g}} \tag{11}$$

where $\mathbf{r}$ is the vector location of the cg and can be solved for by rewriting Eq. (11) in matrix from:

$$\mathbf{B}\mathbf{u} = \mathbf{z} \tag{12a}$$

$$\mathbf{B}_{(k)} = \begin{bmatrix} 0 & f_{z(k)} & -f_{y(k)} & 1 & 0 & 0 \\ -f_{z(k)} & 0 & f_{x(k)} & 0 & 1 & 0 \\ f_{y(k)} & -f_{x(k)} & 0 & 0 & 0 & 1 \end{bmatrix} \tag{12b}$$

$$\mathbf{u} = \begin{bmatrix} r_x, r_y, r_z, o_{xx}, o_{yy}, o_{zz} \end{bmatrix}^{\mathrm{T}} \tag{12c}$$

$$\mathbf{z}_{(k)} = \begin{bmatrix} \tilde{m}_{x(k)}, \tilde{m}_{y(k)}, \tilde{m}_{z(k)} \end{bmatrix}^{\mathrm{T}} \tag{12d}$$

The mass of the tool, its cg, and the bias vector are fed forward for all subsequent load cell measurements:

$${}^s\bar{\mathbf{w}} = {}^s\tilde{\mathbf{w}} - {}^s\mathbf{o} - mg \begin{bmatrix} {}^s\hat{\mathbf{g}} \\ {}^s\mathbf{r} \times {}^s\hat{\mathbf{g}} \end{bmatrix} \tag{13}$$

which ideally will give ${}^s\bar{\mathbf{w}} = 0$ for any orientation within the robot's workspace with a zero input wrench. It should be noted this method does not account for the dynamic effects of the tool mass, however, the target application of this system requires motion profiles on the order of magnitude of several $\frac{\mu\text{m}}{\text{s}}$ in which case it is reasonable to assume negligible dynamic effects.

REFERENCES

[1] M. A. Parker, L. R. Erker, I. Audo, D. Choi, S. Mohand-Said, K. Sestakauskas, P. Benoit, T. Appelqvist, M. Krahmer, C. Ségaut-Prévost *et al.*, "Three-year safety results of sar422459 (eiav-abca4) gene therapy in patients with abca4-associated stargardt disease: An open-label dose-escalation phase i/iia clinical trial, cohorts 1-5," *American Journal of Ophthalmology*, 2022.

[2] R. Ladha, L. E. Caspers, F. Willermain, and M. D. de Smet, "Subretinal therapy: Technological solutions to surgical and immunological challenges," *Frontiers in Medicine*, vol. 9, 2022.

[3] E. Z. Ahronovich, N. Simaan, and K. M. Joos, "A review of robotic and oct-aided systems for vitreoretinal surgery," *Advances in therapy*, vol. 38, no. 5, pp. 2114–2129, 2021.

[4] I. I. Iordachita, M. D. De Smet, G. Naus, M. Mitsuishi, and C. N. Riviere, "Robotic assistance for intraocular microsurgery: Challenges and perspectives," *Proceedings of the IEEE*, vol. 110, no. 7, pp. 893–908, 2022.

[5] M. D. de Smet, T. C. Meenink, T. Janssens, V. Vanheukelom, G. J. Naus, M. J. Beelen, C. Meers, B. Jonckx, and J.-M. Stassen, "Robotic assisted cannulation of occluded retinal veins," *PloS one*, vol. 11, no. 9, p. e0162037, 2016.

[6] J. T. Wilson, M. J. Gerber, S. W. Prince, C.-W. Chen, S. D. Schwartz, J.-P. Hubschman, and T.-C. Tsao, "Intraocular robotic interventional surgical system (iriss): Mechanical design, evaluation, and master–slave manipulation," *The International Journal of Medical Robotics and Computer Assisted Surgery*, vol. 14, no. 1, p. e1842, 2018.

[7] W. Wei, R. Goldman, N. Simaan, H. Fine, and S. Chang, "Design and theoretical evaluation of micro-surgical manipulators for orbital manipulation and intraocular dexterity," in *Proceedings 2007 IEEE international conference on robotics and automation*. IEEE, 2007, pp. 3389–3395.

[8] R. A. MacLachlan, B. C. Becker, J. C. Tabarés, G. W. Podnar, L. A. Lobes, and C. N. Riviere, "Micron: an actively stabilized handheld tool for microsurgery," *IEEE transactions on robotics*, vol. 28, no. 1, pp. 195–212, 2011.

[9] B. J. Nelson, I. K. Kaliakatsos, and J. J. Abbott, "Microrobots for minimally invasive medicine," *Annual review of biomedical engineering*, vol. 12, pp. 55–85, 2010.

[10] A. Üneri, M. A. Balicki, J. Handa, P. Gehlbach, R. H. Taylor, and I. Iordachita, "New steady-hand eye robot with micro-force sensing for vitreoretinal surgery," in *2010 3rd IEEE RAS & EMBS International Conference on Biomedical Robotics and Biomechatronics*. IEEE, 2010, pp. 814–819.

[11] A. Gijbels, N. Wouters, P. Stalmans, H. Van Brussel, D. Reynaerts, and E. Vander Poorten, "Design and realisation of a novel robotic manipulator for retinal surgery," in *2013 IEEE/RSJ International Conference on Intelligent Robots and Systems*. IEEE, 2013, pp. 3598–3603.

[12] E. Vander Poorten, C. N. Riviere, J. J. Abbott, C. Bergeles, M. A. Nasseri, J. U. Kang, R. Sznitman, K. Faridpooya, and I. Iordachita, "Robotic retinal surgery," in *Handbook of Robotic and Image-Guided Surgery*. Elsevier, 2020, pp. 627–672.

[13] C. Song, P. L. Gehlbach, and J. U. Kang, "Active tremor cancellation by a "smart" handheld vitreoretinal microsurgical tool using swept source optical coherence tomography," *Optics express*, vol. 20, no. 21, pp. 23 414–23 421, 2012.

[14] J. U. Kang and G. W. Cheon, "Demonstration of subretinal injection using common-path swept source oct guided microinjector," *Applied Sciences*, vol. 8, no. 8, p. 1287, 2018.

[15] M. Ourak, J. Smits, L. Esteveny, G. Borghesan, A. Gijbels, L. Schoevaerdts, Y. Douven, J. Scholtes, E. Lankenau, T. Eixmann *et al.*, "Combined oct distance and fbg force sensing cannulation needle for retinal vein cannulation: in vivo animal validation," *International journal of computer assisted radiology and surgery*, vol. 14, no. 2, pp. 301–309, 2019.

[16] H. Yu, J.-H. Shen, R. J. Shah, N. Simaan, and K. M. Joos, "Evaluation of microsurgical tasks with oct-guided and/or robot-assisted ophthalmic forceps," *Biomedical optics express*, vol. 6, no. 2, pp. 457–472, 2015.

[17] H. Yu, J.-H. Shen, K. M. Joos, and N. Simaan, "Calibration and integration of b-mode optical coherence tomography for assistive control in robotic microsurgery," *IEEE/ASME Transactions on Mechatronics*, vol. 21, no. 6, pp. 2613–2623, 2016.

[18] G. Del Giudice, A. L. Orekhov, J.-H. Shen, K. M. Joos, and N. Simaan, "Investigation of micromotion kinematics of continuum robots for volumetric oct and oct-guided visual servoing," *IEEE/ASME Transactions on Mechatronics*, vol. 26, no. 5, pp. 2604–2615, 2020.

[19] K. M. Joos and J.-H. Shen, "Miniature real-time intraoperative forward-imaging optical coherence tomography probe," *Biomedical optics express*, vol. 4, no. 8, pp. 1342–1350, 2013.

[20] Y. Nakamura and H. Hanafusa, "Inverse kinematic solutions with singularity robustness for robot manipulator control," 1986.

[21] G. Del Giudice, A. Orekhov, J. Shen, K. Joos, and N. Simaan, "Investigation of micro-motion kinematics of continuum robots for volumetric oct and oct-guided visual servoing," *IEEE/ASME Transactions on Mechatronics*, pp. 1–1, 2020.

[22] J. Pile, "Wire-actuated parallel robots for cochlear implantation with in-vivo sensory feedback," Ph.D. dissertation, Dept. of Mech. Eng., Vanderbilt Univ., Nashville, TN, USA, 2015.